Research Article
doi.org/10.1002/elsa.202100224

Chemistry Europe
European Chemical Societies Publishing

Received: 31 December 2021
Revised: 19 April 2022
Accepted: 11 June 2022

Designing multinary noble metal-free catalyst for hydrogen evolution reaction

Wissam A. Saidi[1] | **Tarak Nandi**[2] | **Timothy Yang**[1]

[1]Department of Mechanical Engineering and Materials Science, University of Pittsburgh, Pittsburgh, Pennsylvania, USA

[2]Independent Researcher, Morgantown, West Virginia, USA

Correspondence
Wissam A. Saidi, Department of Mechanical Engineering and Materials Science, University of Pittsburgh, Pittsburgh, PA 15261, USA.
Email: alsaidi@pitt.edu

Abstract

The hydrogen evolution reaction (HER), the key reaction for electrocatalytic production of hydrogen, is of fundamental importance due to its simplicity yet is very important for renewable energy. Notwithstanding, Pt is still the main catalyst for this reaction, which is not practical for the industrial deployment of this technology owing to the high cost and scarcity of Pt. The successful synthesis of high entropy alloy (HEA) nanoparticles opens a new frontier for the development of new catalysts. Herein we investigate the design of a multinary noble metal-free HER catalyst based on earth-abundant elements Co, Mo, Fe, Ni, and Cu. Using a machine learning (ML) approach in conjunction with first-principles methods, we build a model that can rapidly compute the hydrogen adsorption energy on the alloyed surfaces with high fidelity. Within the large composition space of the CoMoFeNiCu HEA, a large number of alloy combinations are shown to optimally bind hydrogen with a high probability. Further, most of these alloy compositions are found stable against dissociation into intermetallics, and hence synthesizable as a solid solution, by virtue of a large mixing entropy compared to mixing enthalpy and a small lattice mismatch between the elements. This finding is partly consistent with recent experimental results that synthesized five different CoMoFeNiCu HEA compositions. Our study underscores the significant impact that computational modeling and ML can have on developing new cost-effective electrocatalysts in the nearly-infinite materials design space of HEAs, and calls for experimental validation.

KEYWORDS
density functional theory, high entropy alloys, hydrogen evolution reaction, machine learning

1 | INTRODUCTION

The hydrogen economy is a promising route to phase out the global energy dependence on the combustion of fossil fuels, and hence mitigate climate changes. Electrocatalysts hold a prominent role in this economy as they can increase the rate, efficiency, and selectivity for the hydrogen evolution reaction (HER), the fundamental reaction for producing $H_2(g)$.[1] Unfortunately, HER requires an expensive electrocatalyst, primarily platinum, in order to produce describable amounts of energy, which severely limits its practicality for industrial applications. One of the

Research Article
doi.org/10.1002/elsa.202100224
Chemistry Europe
European Chemical Societies Publishing

main challenges in the hydrogen economy is to develop HER electrocatalysts that require lesser amounts of Pt or in finding completely different cost-effective alternatives.[2–5]

High entropy alloys (HEAs) are multiple principal element alloys that are attracting increased interest in the field of catalysis as they recently became amenable for synthesis as nanoparticles with different compositions.[6–11] Initial findings in this strongly evolving field suggest that HEAs may in particular enable the design and synthesis of novel catalysts with higher activity, lower cost, or both.[12–17] For example, CrMnFeCoNi HEA is demonstrated to have an intrinsic electrocatalytic activity for oxygen reduction which exceeds that of the precious metal Pt.[13] AuAgPtPdCu HEAs are shown to be efficient catalysts for the electrochemical reduction of CO_2.[8,14] CoMoFeNiCu HEAs are found to decompose ammonia 20 times more efficiently than the state-of-the-art precious-metal Ru catalysts.[17]

For many reactions, catalysts design has often relied on first-principles theoretical calculations, which predict the HER activities of new catalysts on a volcano plot based on a relatively easy-to-compute descriptor(s). For instance, the hydrogen binding energy has been shown to be a good descriptor for HER where the optimal catalysts such as Pt neither bind hydrogen too strongly nor too weakly. In addition, the descriptor can be applied to accurately predict the exchange currents for catalysts measured in experiments.[18–20] However, the study of alloyed surfaces, particularly the complex HEAs pose a significant challenge to theoretical calculations.[21] This is because the theory of catalysis requires the evaluation of the binding strength of different adsorbates on the surface, which is not easy to compute for alloyed surfaces owing to a large number of surface sites with different chemical environments. Recently, several studies have shown that machine learning (ML) approaches can accelerate the computation of the adsorption energies on surfaces.[22–28] Particularly a notable study by Rossmeisl and coworkers applied a relatively simple ML approach to show that the adsorption energy in HEAs can be described well based on the number of different chemical species in the local environment of the adsorption site.[8,29] Also, Saidi and collaborators have shown that a deep learning ML approach can obtain high fidelity adsorption energies on HEA surfaces.[30,31]

Another challenge in modeling HEAs is in quantifying their catalytic activity given that alloy surfaces have a large number of chemical environments with different adsorption energies. Although while very likely that some of these sites would be optimum for a given chemical reaction, this does not necessarily imply that the HEA is a good catalyst for that reaction because the probability of realizing these environments could be low on the surface. The recent study by Rossmeisl and collaborators introduced the average adsorption energy of the HEA computed by averaging a large number of different sites on the HEA surface, as a criterion to quantify the activity of the surface.[29] This probabilistic approach for defining the chemical activity of the HEA has been utilized to predict optimum compositions of HEA catalysts for CO_2 reduction[8,14] and also for ammonia decomposition[17,30] based on utilizing a single descriptor for these reactions. The success of the probabilistic approach could be attributed to the emergence of scaling relationships between the configurations-averaged adsorption energies that are absent for the adsorption energies.[32] Herein, we also apply the probabilistic approach based on the average hydrogen adsorption energy to design a HEA CoMoFeNiCu HER catalyst. We show that there is a relatively large number of potential compositions that can bind hydrogen similar to that of Pt, which is a necessary condition for having an optimum HER catalyst. Further, we show that a large number of these potential catalysts are stable in the HEA phase, hence synthesizable, which calls for experimental validation.

2 | RESULTS AND DISCUSSION

2.1 | Stability of the HEA phase

Before we discuss the catalytic activity of the CoMoFeNiCu alloy it is useful to first assess the stability of the alloy against the undesirable ordered intermetallics and dissociation into multiple phases. Experimentally, CoMoFeNiCu HEA was synthesized with five different alloy compositions, namely $Co_xMo_yFe_{10}Ni_{10}Cu_{10}(x{+}y = 70)$ where the atomic ratio of Co/Mo is varied as 15/55, 25/45, 35/35, 45/25, and 55/15.[17] To investigate the thermodynamic stability of the alloy for different compositions, we inspect δr, ΔS_{mix}, and ΔH_{mix}. $\delta r = \sum_{i,j}^{5} c_i c_j (r_i - r_j)$ is the difference in atomic radius between the elements in the alloy weighted by the concentration c_i $(i = 1, 5)$ of the elements, $\Delta S_{\text{mix}} = -k_B \sum_i^5 c_i \ln c_i$ is the ideal mixing entropy (where $k_B$is the Boltzmann constant), and ΔH_{mix} is the mixing enthalpy. For a given temperature T, if the entropic term ΔS_{mix} is larger than $|\Delta H_{\text{mix}}|/T$, then it is expected that the solid solution phase of the alloy will be more stable than the ordered intermetallics. Further, it is expected that as the lattice mismatch δr increases, then also the HEA phase will be less stable due to increased strain effects, akin to Vegard's law for binary alloys. Empirically, it is found that generally, the HEA phase is stable if $\Omega = \frac{T_m \, \Delta S_{\text{mix}}}{|\Delta H_{\text{mix}}|} > 1.1$ and $\delta r < 6.6\%$ where $T_m = \sum_i^5 c_i \, T_m^i$ is the melting temperature of the alloy approximated from the rule of mixtures.[33,34]

Research Article
doi.org/10.1002/elsa.202100224
Chemistry Europe
European Chemical Societies Publishing

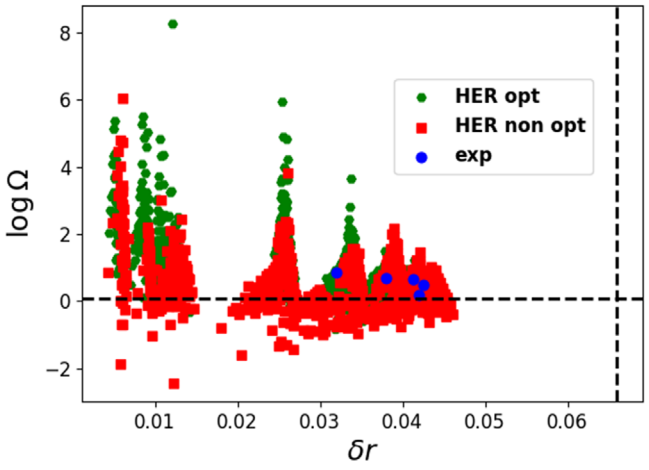

FIGURE 1 Variations of Ω and δr for 1800 different alloy compositions. The dashed horizontal and vertical lines correspond to Log (1.1) and 0.066, respectively. Alloys located in the upper left corner above the horizontal Log (1.1) line and to the left of the vertical 0.066 are expected to be stable. Data labeled 'HER opt' and 'HER non opt' indicate compositions that are optimum (not optimum) for hydrogen evolution reaction (HER). Data labeled 'exp' correspond to the compositions that were synthesize recently[17]

We have computed the values for Ω and δr for 1800 different alloy compositions. Rather than using the empirical formula ΔH_{mix} proposed before based on the binary alloy systems and alloy concentrations,[33,34] we instead computed ΔH_{mix} directly from density functional theory (DFT) as done before.[29] Namely, for each composition, we computed ΔH_{mix} by averaging the enthalpies of five different random configurations of the alloy. Herein we assumed that the alloys adapt an fcc lattice regardless of their composition, which has been verified experimentally for five different compositions.[17] Values for Ω and δr are summarized in Figure 1.

Figure 1 shows that the lattice mismatch δr is less than the 6.6% limit for all the investigated alloy compositions, suggesting the stability of the HEA phase against the lattice mismatch criterion. The values for Ω vary in a wider range but most alloys have values greater than 1.1. This suggests that CoMoFeNiCu HEAs are generally synthesizable regardless of their composition. For instance, as a validation, we also computed Ω and δr for the CoMoFeNiCu HEA alloys that were synthesized recently.[17] As shown in Figure 1, these alloys are in the upper left region such that $\Omega > 1.1$ and $\delta r < 6.6\%$, suggesting that HEA phase stability according to the empirical criteria, as they should be. Although our assessment of the synthesizability as a solid solution is empirical in nature, the agreement with experimental results lends further credibility to these rules. Also, for completeness, we note that the stability investigations of the HEA NPs in vacuum could be different from their stability under electrochemical conditions.

We next investigate the interactions of hydrogen with the alloyed surfaces. Pt (111) is the best single metal catalyst for HER[35] that binds H with energy of –0.48 eV/H based on our computational framework. Herein, as a guiding principle, we will assess the HER catalytic activity of the alloy in reference to Pt (111) where the alloy composition is optimum if the average adsorption energy of *H is equivalent to that of Pt (111). One advantage of comparing with respect to Pt (111) rather than the absolute *H adsorption energy value is that the results would be less sensitive to intrinsic errors in the underlying DFT computational framework. For instance, the difference in binding energy between Au and Pt is 0.61 eV for both the conventional[36] and revised[37] Perdew-Burke-Ehrenzhof exchange-correlation functionals despite the different absolute values for both metals.

To illustrate hydrogen interactions with the alloyed surface, we examined the binding sites of H on 3 different HEA surfaces. Because of the random nature of the surface sites, all adsorption sites that even have the same site symmetry are expected to be different, which is unlike the case of pure metal slabs where these would be the same. For instance, for the model shown in Figure S1, we find that 4 different fcc adsorption energies –0.28, –0.39, –0.51 and –0.58 eV/H and 4 different hcp energies –0.30, –0.40, –0.50 and –0.56 eV/H. For this model, the two most stable adsorption sites are neighboring Fe atoms while the weakest sites are neighbor Cu atoms. Also, similar to the pure metal slabs, the 3-metal coordinated hollow sites are found to have the lowest energies while all atop or bridge sites were not stable.

Because hydrogen interactions are negligible, the adsorption strength of single hydrogen at all potential surface sites would suffice to characterize the surface reactivity to a very good approximation. This conclusion can be drawn from studying the coverage dependence of the hydrogen adsorption strength on different surfaces.[38] As shown in this study, for surfaces with moderate to strong interactions with hydrogen, the *H adsorption energies differ by less than 0.1 eV for hydrogen coverage between 1/4 and one monolayer. The 0.1 eV is expected to be on par with the accuracy of the ML model, as discussed later. Even though H interactions could modulate the adsorption strength by up to 0.2 eV on the less reactive Cu and Au surfaces, we do not expect this to affect our findings that are focused on surfaces that bind H optimally, as for the case of Pt. Additionally, for such surfaces, the rate-determining step for the HER is expected to be Heyrovsky or Volmer reactions considering that thermodynamic accessibility dominates the kinetic behavior's properties.[39] Thus, only one hydrogen atom or one active site is involved in each reaction pathway. In contrast, if the rate-determining step is the Tafel reaction as in Pt (111),

Research Article
doi.org/10.1002/elsa.202100224
Chemistry Europe
European Chemical Societies Publishing

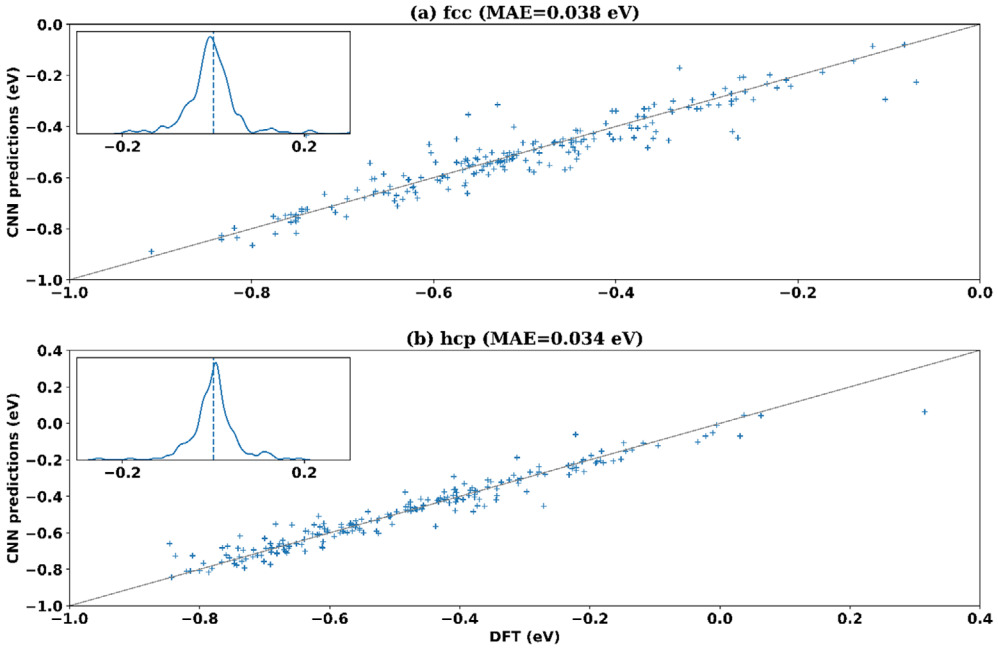

FIGURE 2 Comparison between *H adsorption energy predictions based on convolutional neural network (CNN) and DFT ground truth values for the testing set for (a) fcc and (b) hcp sites. The inset shows the distribution in the differences between the machine learning (ML) and density functional theory (DFT) values, and the mean absolute error (MAE) for the overall accuracy of the model

two surface hydrogen atoms are involved for each reaction pathway.[35] Indeed even for the high active metals such as Pt, Ir, Rh, and Pd, the rate-determining steps are tested to be the Volmer step experimentally.[40]

The applied straightforward DFT approach for examining hydrogen interactions on the HEA surfaces cannot be applied to compute the adsorption energy of all potential configurations of the HEA alloy. To address this challenge, we developed ML models to rapidly compute the *H adsorption energies using as input easy-to-compute features to characterize the surface configuration. The ML models are trained using a database of ∼4000 different adsorption configurations of *H that differ in the alloy composition, arrangement of the atoms, as well as the metal sites that interact with H. The initial configurations are created by depositing H at either fcc or hcp hollow metal sites and then optimizing the geometry. We found that predominantly the final geometries mostly retain the site symmetry of the initial configurations. We utilized the developed database to train site-specific ML models for the fcc and hcp configurations.

We applied four different ML models: one based on a convolutional neural network (CNN), and three tree-based models (decision tree, random forest, and gradient boosted decision trees). Overall, the four different ML models behaved similarly although the CNN model was found to be more robust and incorporates the spatial features corresponding to the atomic arrangements into the training procedure. The CNN model was adopted as the primary model for our analysis. Figure 2 compares the adsorption energies for the test dataset (which contains 10% of the total dataset and was not used during the model training process) obtained from the CNN model predictions and from the DFT calculations (similar parity plots are shown for the other ML models in Figures S3–S5). For the fcc and hcp site symmetries, it can be observed that the data points are clustered around the 45° reference line (solid line) indicating a strong similarity between the ML predictions and the DFT calculations, with the differences quantified using the mean absolute error that is of similar magnitude to the intrinsic errors of the employed DFT functional. The insets in the figures show that no appreciable bias is present in the distribution of the ML prediction errors around their mean value. To understand the robustness of the methodology employed against the inherent variability in the dataset, the model training/testing was repeated using four different splits of the dataset. The magnitude and distribution of the errors were found to be similar among the four cases, as shown in Figure S2 for the fcc dataset. The above observations support the reliability of the chosen CNN hyperparameters and the training methodology and give the confidence to use the trained model for obtaining predictions for completely new datasets.

Using the developed ML model, we compute the average adsorption energy $\widehat{\Delta E}$ for a wide range of alloy compositions. As discussed in the introduction, it is the average adsorption energy that quantifies the most

Research Article
doi.org/10.1002/elsa.202100224
Chemistry Europe
European Chemical Societies Publishing

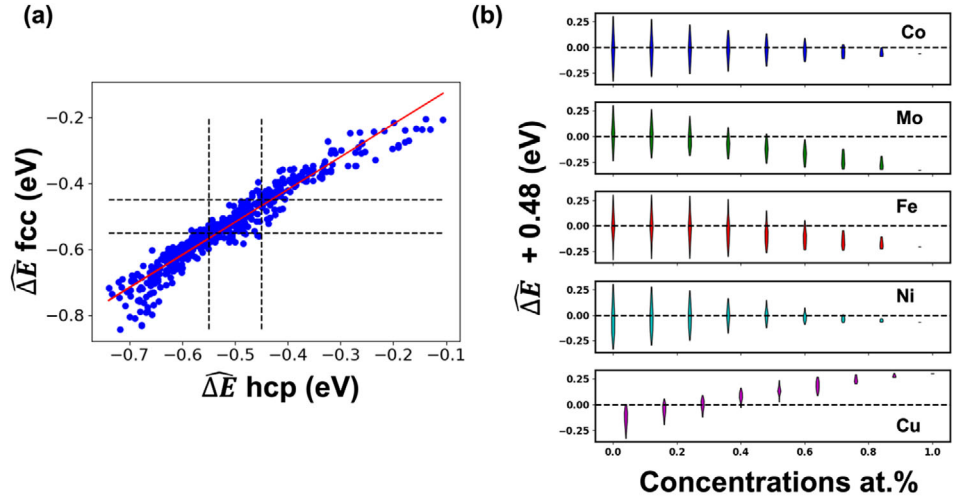

FIGURE 3 (a) Correlations between $\widehat{\Delta E}$ for *H at fcc and hcp sites. The red line corresponds to linear dependence with predictivity coefficient $r^2 = 0.96$. (b) Variations of $\widehat{\Delta E}$ with elements compositions. For convenience, we shifted $\widehat{\Delta E}$ by −0.48 eV so the zero value indicates catalysts that bind *H optimally as in Pt

probable adsorption energy on the surface, and hence can be used to assess the catalytic efficiency.[29] We utilize $n_s = 3000$ different adsorption configurations for each alloy composition and compute the average adsorption $\widehat{\Delta E} = \sum_{\ell}^{n_s} f_\ell \Delta E_\ell / \sum_{\ell}^{n_s} f_\ell$ where $f = \prod_k^4 {c_k}^{N_k}$ measures the number of possibilities of generating a surface microstructure with N_k metal atoms consistent with HEA composition c_k (omitting label ℓ for clarity).[8,29] This approach is equivalent to using a surface with 3000×3000 sites. Figure 3 summarizes $\widehat{\Delta E}$ for *H on either fcc or hcp sites. HEAs with $\widehat{\Delta E} = -0.48$ eV on average bind *H similar to that of Pt (111) and hence are expected to be good HER catalysts. As can be seen from the figure, there is a large number of alloy compositions that satisfy this constraint.

To better understand the constraints on the compositions of the HER activity, we show in Figure 3b how $\widehat{\Delta E}$ varies with the 5 different elements' compositions. For instance, this figure shows that optimum HEA alloys can have a wide range of ∼0–80 at% of Co or Ni. On the other hand, the range is narrower for Fe (0%–60%), Mo (0%–40%), and Cu (20–40%) at%.

These trends can be somewhat rationalized by inspecting the *H adsorption energies on the pure metal surfaces. Namely, the *H hcp adsorption energies on the fcc(111) pure metal surfaces for Co, Mo, Fe, Ni, and Cu are −0.50, −1.08, −0.81, −0.58, and −0.30 eV/H, respectively. The fcc adsorption energies are of similar magnitude except for Mo where it is −1.52 eV/H. For the pure metal surfaces Co, Fe, and Mo, we chose to examine the fcc lattice rather than the ground state configuration to better compare with the HEA results. From the pure metal surfaces, not surprisingly, the adsorption strength of *H to the HEAs surfaces increases (becoming less negative) as the Mo and Fe contents increase. On the other hand, we see the opposite behavior with the increase of Cu considering that Cu(111) *H binding is significantly weaker than the rest of the metals. The trends of $\widehat{\Delta E}$ with the Co and Ni concentrations increase is similar, also in agreement with the pure metals case.

To further understand the nature of the catalytic site, we examined the chemical composition of the *H local environment. For the five different metals, there are 35 different variations for the three metal atoms that are the first nearest neighbors to H. Using the 5.4 million local environments obtained from sampling 1800 alloy compositions each with 3000 configurations, we examined the distribution of the binding energies for the different environments. Figure 4 summarizes the obtained mean and standard deviation of the binding energies. For instance, the MoMoMo local environment yields the most stable adsorption site with an average adsorption energy of −0.75 eV/H for hcp and −0.85 eV/H for fcc, while CuCuCu has the weakest with adsorption energy ∼-0.2 eV/H, as can be expected from the behavior of the corresponding pure metal surfaces. As seen from the figure there are different local environments that bind *H optimally such that $|\widehat{\Delta E} + 0.48| < 0.05$ eV including CoCoCu, CoCoNi, CoCuMo, CoNiNi, FeCoCu, FeFeCu, FeNiNi, NiCuMo, NiNiNi, FeFeCu, CoCuMo, and CoCuMo.

The above analyses suggest that there is a large number of potential noble metal-free CoMoFeNiCu that bind hydrogen optimally as in Pt (111). Further, Figure 1 shows that a large number of these optimum compositions are expected to be synthesizable based on the empirical Ω and δr rules. Table S1 summarizes these stable and potential HER catalysts.

Research Article
doi.org/10.1002/elsa.202100224
Chemistry Europe
European Chemical Societies Publishing

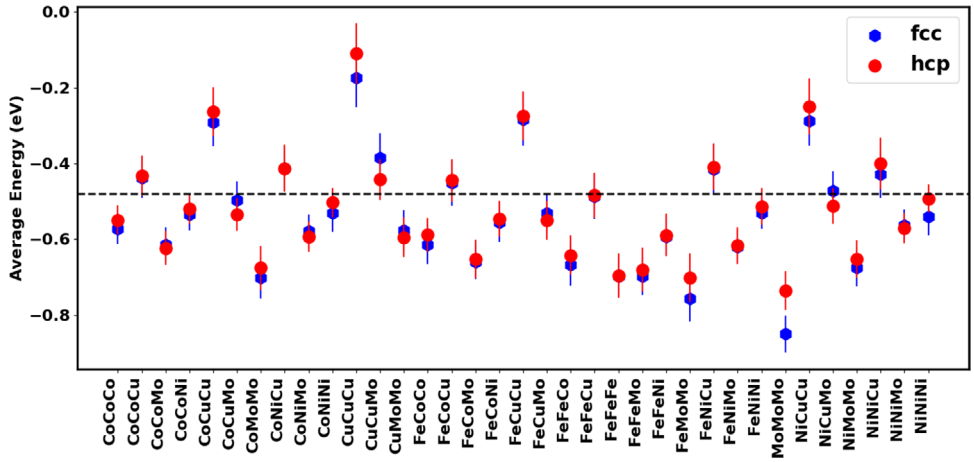

FIGURE 4 Breakup of the adsorption energies based on the site's symmetry. The horizontal line shows the optimum value of –0.48 eV for Pt (111)

3 | CONCLUSION

The study of the alloyed surface is a major challenge to the theory of catalysis based on traditional first-principles calculations owing to their lack of periodicity. In this respect, HEAs are an extreme example and a seminal challenge owing to the enormous number of different chemical environments. We show that the study of HEA surfaces is trackable using a combined approach based on DFT and accelerated with ML, and can provide adsorption energies with errors that are commensurate with the intrinsic errors of DFT. We have applied the combined DFT/ML approach to study hydrogen interactions on CoMoFeNiCu fcc(111) surfaces. We show that there is a wide range of alloy compositions that with a high probability can bind hydrogen equivalently to that of Pt (111). This strongly suggests that these surfaces can be optimum catalysts for HER. Our findings predict that HEAs made of earth-abundant metals can replace the precious Pt to activate HER and call for experimental validation.

4 | EXPERIMENTAL SECTION

4.1 | First-principles computational approach

The first-principles calculations are carried out using the Perdew-Burke-Ehrenzhof exchange-correlation functional[37] as employed in the Vienna Ab initio Simulation Package. We used the projector augmented wave pseudopotentials to model the electron-nucleus interactions.[41,42] The slab models of the fcc (111) HEA surface are studied using a 2×2 surface supercell with 5 layers of atoms, and 10 Å to mitigate interactions along the non-periodic direction. The previous experimental study that synthesized CoMoFeNiCu HEA NPs reported the observation of the (111) surface termination,[17] and hence the focus on this termination to study the NPs is a good approximation. The Kohn-Sham orbitals are expanded using a 300 eV plane-wave cutoff. The Brillion zone is sampled using a 3×3×1 shifted Monkhorst-Pack grid with 0.2 eV Gaussian smearing. All calculations are spin-polarized, which is needed to account for the magnetic elements. During geometry relaxation, all atoms including the top two metal layers and hydrogen adsorbates are relaxed using a force tolerance of 0.1 eV/Å. Lattice constants of the HEAs are obtained as a weighted average based on the alloy composition, following Vegard's law for binary alloys.

The hydrogen adsorption energy ΔE is calculated as, $\Delta E = E_{*H} - E^* - 0.5\, E_{\mathrm{H2}}$ where E_{*H} is the energy of the relaxed slab with the adsorbed hydrogen, E^* is the energy of the relaxed pure surface, and E_{H2} is the energy of the H_2 molecule computed using a cubic supercell approach with a 10 Å side.

To assess the stability of the alloy, we have computed the mixing enthalpy ΔH_{mix} by optimizing 2×2×2 bulk supercells of the conventional fcc lattice (32 atoms) and measuring its energy with respect to the bulk reference configurations. Namely, we used $\Delta H_{\mathrm{mix}} = E_{\mathrm{alloy}} - \sum_i^5 c_i E_i^{\mathrm{ele}}$ where E_{alloy} is the total energy of the alloy and $E_i^{\mathrm{ele}} (i = 1 - 5)$ are the bulk metal energies. We used a 3×3×3 shifted Monkhorst-Pack grid with 0.2 eV Gaussian smearing for the bulk calculations, consistent with that used k-grid for the slabs. We averaged ΔH_{mix} over 5 different random structures consistent with the alloy composition.

Research Article
doi.org/10.1002/elsa.202100224
Chemistry Europe
European Chemical Societies Publishing

4.2 | Feature selection

The training database for the ML models is based on ~4000 different adsorption energies obtained from random configurations. The feature representation of each configuration encodes information about the physical properties of the metals and their locations with respect to the adsorption site. The physical properties include element-specific features (ionization energy, electronegativity, electron affinity, and a number of valence electrons), in addition to metal-specific features (Wigner-Seitz radius r_s, d-band center $\in_d$, d-band filling f_d, coupling matrix elements between adsorbate and metal d-states V_{ad}, $d\ln \in_d / d\ln r_s$, and work function). Thus, in total, we have 11 features per site. In addition, we include also a 5-element vector to characterize the overall composition of the alloy. The geometrical information of the metals corresponds to the location of the sites with respect to the adsorption site. Thus, for each configuration, we include (three layers) x (four atoms/layer) x (11 features/site) + (five composition vectors) = 137 features.

4.3 | Machine learning

We explore four different ML approaches for this study. One is based on a CNN, and three tree-based models, namely decision tree, random forest, and gradient boosted decision trees. The hyperparameters of the tree-based models were chosen using a Bayesian search technique along with k-fold cross validation. A pre-defined hyperparameter search space was explored in an efficient manner to arrive at the set of hyperparameters that led to the lowest mean cross validation loss over the training dataset.

4.3.1 | Convolutional neural network

CNN is a specialized type of neural network capable of efficiently handling data that have 2D/3D arrangements and can incorporate spatial relationships inherent in the dataset into the learning process. For this work, we employ a CNN-based model that utilizes the information about the relative arrangement of the atoms around the binding location for obtaining the predictions. Unlike a standard fully-connected neural network, the layers in a CNN have neurons arranged in multiple dimensions, and any neuron in a convolutional layer is connected only to a small set of neurons in the previous layer. This arrangement can drastically reduce the total number of model parameters to be learned during the training process. The fundamental operation in a CNN is the convolution operation (represented by $*$ in the equation below) that involves the calculation of the output of a neuron in a given convolutional layer l, at a location with indices i and j (assuming a 2D arrangement of input data and neurons), represented by $S(i, j)$, using the corresponding *receptive field* in layer *l-1*, and a learnable *kernel* (also referred to as a *filter*), K [43]

$$S(i,j) = (I * K)(i,j) = \sum_m \sum_n I(i+m, j+n) K(m,n). \quad (1)$$

In the above equation, m and n represent the size of the kernel (K) and I is the output of layer *l-1*. Usually, a CNN consists of multiple convolutional layers arranged in a manner that allows hierarchical learning of spatial features in the input data. Often, the convolutional layers are interspersed with *pooling* layers that help further reduce the total number of parameters in the model.

The CNN architecture used here follows our previous study.[28,30] The input layer is followed by two convolutional layers and a fully connected layer that is connected to the output layer that provides the predictions to be used for the loss function calculation. The first convolutional layer uses a one-dimensional kernel (with a size equal to the number of input features) to generate 64 feature maps. The second convolutional layer uses a two-dimensional kernel and 128. The fully connected layer consists of 100 neurons and is followed by a dropout layer with a drop rate of 0.2 to prevent overfitting. All the convolutional and fully connected layers use the ReLU activation function. Max-pooling layers (that downsample the outputs of the previous layers by a factor of 2) are present between the two convolutional layers, and between the second convolutional layer and the fully connected layer. The last layer consists of one neuron that takes the output of the fully connected layer as input and provides the prediction of the adsorption energy.

4.3.2 | Decision tree model

The decision tree model is essentially a univariate binary tree model forming the foundation for the random forest and gradient boosted decision tree models (explained later) that consist of an ensemble of decision trees for improved generalizability. The training step for a decision tree model involves the recursive splitting of the feature space into distinct nonoverlapping high-dimensional rectangular regions. For performing the first binary split, all available features are explored to choose the feature, and the split point corresponding to that feature, that divides the dataset into two regions with the least sum of squared

Research Article
doi.org/10.1002/elsa.202100224

error between the target value for each training instance in a region and the averaged target value for that region. For any feature X_k (where the overall feature space is represented by $\boldsymbol{X}$), if a split point s divides the feature space into two regions R_1 and R_2, where

$$R_1(s, X_k) = \{X | X_k < s\} \quad \text{and} \quad R_2(s, X_k) = \{X | X_k \geq s\}, \tag{2}$$

the training procedure involves the identification of X_k and s that minimizes

$$\sum_i (y_i - \hat{y}_{R1})^2 + \sum_j (y_j - \hat{y}_{R2})^2. \tag{3}$$

Here y_i and y_j represent the target values corresponding to each of the training instances in regions R_1 and R_2, respectively. $\hat{y}_{R1}$ and $\hat{y}_{R2}$ are the averaged values of the targets in the corresponding regions. After the optimal split is identified, the above step is repeated to further split each of the two regions further based on the same criterion as before, and the procedure is continued until a stopping criterion is reached. For obtaining the prediction for any observation, the mean of the target value for the training instances in the region where the observation is located is used. The above algorithm splits the feature space in a tree-like manner, using a series of nodes forming a directional graph, that starts from a single node and has more nodes after each split of the feature space. Each node of the tree represents a test for a split, and the nodes that cannot be split anymore are called "leaves". The tree generated is of "univariate" type as each split is based on a single feature, rather than a combination of features. Some of the important hyperparameters of a decision tree model include i) the depth of the tree, ii) the minimum number of samples a tree node must have before it can be split, and iii) the minimum number of samples a leaf node must have. Decision trees are easily interpretable and are versatile and computationally efficient, but they usually suffer from high variance and are prone to overfitting. Although appropriate tuning of the above parameters can alleviate the problem to some extent, ensemble models (e.g., random forest and gradient boosted decision trees) that consist of multiple decision trees have been shown to significantly reduce overfitting.

4.3.3 | Random forest model

Random Forest models use bootstrapped samples to form multiple decision trees and utilize a randomized feature selection method for reducing the overall variance. Instead of using the whole training dataset, multiple bootstrapped datasets are used to train each decision tree. Also, while searching for the best split at any level, only a subset of the overall set of features is used. These two techniques reduce the correlation among the decision trees resulting in an ensemble model that has much less variance than an individual tree and is much less prone to overfit. The prediction for an observation is obtained from the averaged predictions from the relevant constituent decision trees. The random forest model includes all the hyperparameters of a decision tree model, as well as some additional ones relevant to the ensemble process, the major among them being i) the number of decision trees to be used, and ii) the maximum number of features to consider when searching for the best split.

4.3.4 | Gradient boosted decision tree model

While random forest builds multiple decision trees simultaneously and independently, models based on the boosting technique, like the gradient boosted decision trees model, build the trees sequentially. Each tree is built using information from previously grown trees and is trained on the residual errors of the previous tree. The prediction for an observation is obtained from the last decision tree in the sequence of trees. Just like the random forest model, the gradient boosted decision trees model includes all the hyperparameters of a decision tree model, as well as some additional ones relevant for the ensemble process, the major among them being i) the number of decision trees to be used, and ii) the rate at which the boosting progress, that is, the contribution of each new decision tree added to the sequence of trees. For the present work, XGBoost, a highly optimized and robust implementation of the gradient boosted decision trees model is used. XGBoost uses an efficient algorithm for identifying the best split, and other techniques to speed up the training process.

AUTHOR CONTRIBUTIONS

Tarak Nandi contributed to the machine learning analysis and disucssions.

Timothy Yang contributed to the HER analysis and discussions.

ACKNOWLEDGMENTS

W.A.S. and T.Y. are grateful for funding provided by the U. S. National Science Foundation (Award Nos. CSSI-2003808 and CBET-213080). Also, we are grateful for computing time provided in part by the Pittsburgh Center for Research Computing (CRC) resources at the University of Pittsburgh and Argonne Leadership Computing Facility, a DOE

Office Science User Facility supported under Contract DE-AC02-06CH11357.

CONFLICT OF INTEREST

The authors declare that they have no conflict of interest.

DATA AVAILABILITY STATEMENT

The data that support the findings of this study are available from the corresponding author upon reasonable request.

REFERENCES

1. M. S. Dresselhaus, I. L. Thomas, *Nature* **2001**, *414*, 332.
2. National Academies of Sciences, Engineering, and Medicine. *Advances, Challenges, and Long-Term Opportunities in Electrochemistry: Addressing Societal Needs: Proceedings of a Workshop—in Brief* (Ed. E. Mantus), The National Academies Press, Washington, DC **2020**.
3. T. T. Yang, W. A. Saidi, *Nanoscale* **2017**, *9*, 3252.
4. T. T. Yang, W. A. Saidi, *J. Chem. Phys. Lett.* **2020**. *11*, 2759.
5. T. T. Yang, T. L. Tan, W. A. Saidi, *Chem. Mater.* **2020**, *32*, 1315.
6. P.-C. Chen, X. Liu, J. L. Hedrick, Z. Xie, S. Wang, Q.-Y. Lin, M. C. Hersam, V. P. Dravid, C. A. Mirkin, *Science* **2016**, *352*, 1565.
7. C. Chen, Y. Kang, Z. Huo, Z. Zhu, W. Huang, H. L. Xin, J. D. Snyder, D. Li, J. A. Herron, M. Mavrikakis, M. Chi, K. L. More, Y. Li, N. M. Markovic, G. A. Somorjai, P. Yang, V. R. Stamenkovic, *Science* **2014**, *343*, 1339.
8. J. K. Pedersen, T. A. A. Batchelor, A. Bagger, J. Rossmeisl, *ACS Catal.* **2020**, *10*, 2169.
9. B. Song, Y. Yang, T. T. Yang, K. He, X. Hu, Y. Yuan, V. P. Dravid, M. R. Zachariah, W. A. Saidi, Y. Liu, R. Shahbazian-Yassar, *Nano Lett.* **2021**, *21*, 1742.
10. B. Song, Y. Yang, M. Rabbani, T. T. Yang, K. He, X. Hu, Y. Yuan, P. Ghildiyal, V. P. Dravid, M. R. Zachariah, W. A. Saidi, Y. Liu, R. Shahbazian-Yassar, *ACS Nano* **2020**, *14*, 15131.
11. Y. Yao, Z. Huang, P. Xie, S. D. Lacey, R. J. Jacob, H. Xie, F. Chen, A. Nie, T. Pu, M. Rehwoldt, D. Yu, M. R. Zachariah, C. Wang, R. Shahbazian-Yassar, J.u Li, L. Hu, *Science* **2018**, *359*, 1489.
12. T. Löffler, A. Savan, A. Garzã^{3}N-Manjã^{3}N, M. Meischein, C. Scheu, A. Ludwig, W. Schuhmann, *ACS Energy Lett.* **2019**, *4*, 1206.
13. T. Löffler, H. Meyer, A. Savan, P. Wilde, A. Garzã^{3}N Manjã^{3}N, Y.-T. Chen, E. Ventosa, C. Scheu, A. Ludwig, W. Schuhmann, *Adv. Energy Mater.* **2018**, *8*, 1802269.
14. S. Nellaiappan, N. K. Katiyar, R. Kumar, A. Parui, K. D. Malviya, K. G. Pradeep, A. K. Singh, S. Sharma, C. S. Tiwary, K. Biswas, *ACS Catal.* **2020**, *10*, 3658.
15. Y. Xin, S. Li, Y. Qian, W. Zhu, H. Yuan, P. Jiang, R. Guo, L. Wang, *ACS Catal.* **2020**, *10*, 11280.
16. A. Amiri, R. Shahbazian-Yassar, *J. Mater. Chem. A* **2021**, *9*, 782.
17. P. Xie, Y. Yao, Z. Huang, Z. Liu, J. Zhang, T. Li, G. Wang, R. Shahbazian-Yassar, L. Hu, C. Wang, *Nat. Commun.* **2019**, *10*, 4011.
18. J. K. NÃÿRskov, T. Bligaard, A. Logadottir, J. R. Kitchin, J. G. Chen, S. Pandelov, U. Stimming, *J. Electrochem. Soc.* **2005**, *152*.
19. T. T. Yang, R. B. Patil, J. R. McKone, W. A. Saidi, *Catal. Sci. Technol.* **2021**, *11*, 6832.
20. T. T. Yang, W. A. Saidi, *J. Phys. Chem. Lett.* **2022**, *13*, 5310.
21. A. Ferrari, B. Dutta, K. Gubaev, Y. Ikeda, P. Srinivasan, B. Grabowski, F. Kamann, *J. Appl. Phys.* **2020**, *128*, 150901.
22. G. Pilania, A. Mannodi-Kanakkithodi, B. P. Uberuaga, R. Ramprasad, J. E. Gubernatis, T. Lookman, *Sci. Rep.* **2016**, *6*, 19375.
23. L. Ward, A. Agrawal, A. Choudhary, C. Wolverton, *Npj Comput. Mater.* **2016**, *2*, 16028.
24. L. Weston, C. Stampfl, *Phys. Rev. Mater.* **2018**, *2*, 085407.
25. J. Im, S. Lee, T.-W. Ko, H. W. Kim, Y. Hyon, H. Chang, *Comput. Mater.* **2019**, *5*, 37.
26. R. Jose, S. Ramakrishna, *Appl. Mater. Today* **2018**, *10*, 127.
27. K. T. Butler, D. W. Davies, H. Cartwright, O. Isayev, A. Walsh, *Nature* **2018**, *559*, 547.
28. W. A. Saidi, W. Shadid, I. E. Castelli, *Npj Comput. Mater.* **2020**, *6*, 36.
29. T. A. A. Batchelor, J. K. Pedersen, S. H. Winther, I. E. Castelli, K. W. Jacobsen, J. Rossmeisl, *Joule* **2019**, *3*, 834.
30. W. A. Saidi, W. Shadid, G. T. Veser, *J. Phys. Chem. Lett.* **2021**, *12*, 5185.
31. W. A. Saidi, *J. Phys. Chem. Lett.* **2022**, *13*, 1042.
32. W. A. Saidi, W. Shadid, I. E. Castelli, *Npj Comput. Mater.* **2022**, *9*, 36.
33. X. Yang, Y. Zhang, *Mater. Chem. Phys.* **2012**, *132*, 233.
34. Y. Zhang, W. J. Peng, *Proc. Eng.* **2012**, *27*, 1169.
35. E. Skúlason, G. S. Karlberg, J. Rossmeisl, T. Bligaard, J. Greeley, H. Jasson, J. K. Naskov, *Phys. Chem. Chem. Phys.* **2007**, *9*, 3241.
36. J. P. Perdew, K. Burke, M. Ernzerhof, *Phys. Rev. Lett.* **1996**, *77*, 4.
37. J. P. Perdew, K. Burke, M. Ernzerhof, *Phys. Rev. Lett.* **1996**, *77*, 3865.
38. E. Skúlason, V. Tripkovic, M.R. E. Bjãketun, S.ŋD. Gudmundsdãtir, G. Karlberg, J. Rossmeisl, T. Bligaard, H. JÃ^{3}Nsson, J. K. Núskov, *J. Phys. Chem. C* **2010**, *114*, 18182.
39. M. T. Tang, X. Liu, Y. Ji, J. K. Norskov, K. Chan, *J. Phys. Chem. C* **2020**, *124*, 28083.
40. J. Durst, C. Simon, F.D.R. Haschã©, H. A. Gasteiger, *J. Electrochem. Soc.* **2014**, *162*, F190.
41. P. E. Blöchl, *Phys. Rev. B* **1994**, *50*, 17953.
42. G. Kresse, D. Joubert, *Phys. Rev. B* **1999**, *59*, 1758.
43. I. G.a.Y. B.a.A. Courville, *Deep Learning*, MIT Press, Cambridge, MA **2016**,

SUPPORTING INFORMATION

Additional supporting information can be found online in the Supporting Information section at the end of this article.

How to cite this article: W. A. Saidi, T. Nandi, T. Yang. *Electrochem Sci Adv*. **2022**, esa12248. https://doi.org/10.1002/elsa.202100224